Spectroscopic and theoretical investigation of the electronic states of layered perovskite oxyfluoride $Sr_2RuO_3F_2$ thin films

Akira Chikamatsu,[1,*] Yuji Kurauchi,[1] Keisuke Kawahara,[1] Tomoya Onozuka,[1] Makoto Minohara,[2] Hiroshi Kumigashira,[2] Eiji Ikenaga,[3] and Tetsuya Hasegawa[1]

[1]*Department of Chemistry, The University of Tokyo, Tokyo 113-0033, Japan*

[2]*Institute of Materials Structure Science, High Energy Accelerator Research Organization (KEK), Tsukuba, Ibaraki 305-0801, Japan*

[3]*Japan Synchrotron Radiation Research Institute (JASRI)/SPring-8, Mikazuki-cho, Hyogo 679-5198, Japan*

(Received 14 September 2017; revised manuscript received 29 March 2018; published 4 June 2018)

We investigated the electronic structure of a layered perovskite oxyfluoride $Sr_2RuO_3F_2$ thin film by hard x-ray photoemission spectroscopy (HAXPES) and soft x-ray absorption spectroscopy (XAS) as well as density functional theory (DFT)-based calculations. The core-level HAXPES spectra suggested that $Sr_2RuO_3F_2$ is a Mott insulator. The DFT calculations described the total and site-projected density of states and the band dispersion for the optimized crystal structure of $Sr_2RuO_3F_2$, predicting that Ru^{4+} takes a high-spin configuration of $(xy)^{\uparrow}(yz,zx)^{\uparrow\uparrow}(3z^2-r^2)^{\uparrow}$ and that $Sr_2RuO_3F_2$ has an indirect band gap of 0.7 eV with minima at the M, A and X, R points. HAXPES spectra near the Fermi level and the angular-dependent O 1*s* XAS spectra of the $Sr_2RuO_3F_2$ thin film, corresponding to the valence band and conduction band density of states, respectively, were drastically different compared to those of the Sr_2RuO_4 film, suggesting that the changes in the electronic states were mainly driven by the substitution of an oxygen atom coordinated to Ru by fluorine and subsequent modification of the crystal field.

DOI: 10.1103/PhysRevB.97.235101

I. INTRODUCTION

Perovskite-type strontium ruthenates, $Sr_{n+1}Ru_nO_{3n+1}$, where n is the number of layers of corner-sharing RuO_6 octahedra per formula unit, exhibit a rich variety of electric and magnetic properties. The properties of strontium ruthenates are highly sensitive to orbital degrees of freedom, resulting in a strong dependence on the number of RuO_6 octahedral layers in the crystal structure. Nonlayered $SrRuO_3$ with a three-dimensional RuO_6 network is a ferromagnetic metal with a Curie temperature (T_C) of 165 K [1]. On the other hand, single-layered Sr_2RuO_4 and double-layered $Sr_3Ru_2O_7$ are quasi-two-dimensional systems with paramagnetic metallic behavior; the former compound undergoes a spin-triplet superconducting transition below 1.5 K [2–4]. Both the magnetism of $SrRuO_3$ and the superconductivity of Sr_2RuO_4 can be suppressed by substituting isovalent Ca ions for Sr ions, owing to the narrowing of the bandwidth arising from the decrease in the Ru-O-Ru bond angles [5]. The substitution of 3*d* transition-metal ions with 4*d* Ru sites can modify the transport and magnetic properties as well. Doping of 10% of cations containing e_g electrons, such as Mn^{3+}, Co^{2+}, Ni^{2+}, Cu^{2+}, and Zn^{2+}, into $SrRuO_3$ decreased the T_C to 105 K [6,7], due to the narrowing of the Ru $4dt_{2g}$ band induced by the local distortion of RuO_6 octahedra associated with the doping of ions larger than Ru^{4+} and the destructive interaction between the Ru t_{2g} bands via the e_g electrons of the doped cations [6]. In contrast, substitution of 10% Cr^{3+}, which contains only t_{2g} electrons, increased the T_C to 188 K [6,8–11], owing to the widening of the energy bands due to the hybridization of Cr $3dt_{2g}$ and Ru $4dt_{2g}$ orbitals [12].

The electronic properties of strontium ruthenates can also be readily altered by anion doping. For example, $Sr_3Ru^{5+}{}_2O_7F_2$, which was obtained by inserting F^- ions into the $(SrO)_2$ rocksalt blocks in double-layered $Sr_3Ru^{4+}{}_2O_7$ [13], exhibits antiferromagnetism with *G*-type ordering of the Ru^{5+} spins. More recently, $Sr_2RuO_3F_2$ was synthesized in the form of epitaxial thin films by the topotactic fluorination of single-layered Sr_2RuO_4 precursor films using polyvinylidene fluoride (PVDF) [14]. In this reaction, both fluorine insertion into the $(SrO)_2$ blocks and the formation of oxygen vacancies in the O^{2-} sites of the RuO_6 octahedra take place simultaneously, while the oxidation state of Ru remains at 4+ after fluorination. The $Sr_2RuO_3F_2$ thin film exhibits insulating behavior, with a resistivity of $\sim 4.1 \times 10\,\Omega$cm at 300 K, which is five orders of magnitude higher than that of the metallic Sr_2RuO_4 film ($\sim 6.7 \times 10^{-4}\,\Omega$cm). To unveil the origin of the physical properties of $Sr_2RuO_3F_2$, spectroscopic and theoretical approaches to investigate the electronic states of $Sr_2RuO_3F_2$ are highly desirable.

In this study, we investigated the electronic structure of a $Sr_2RuO_3F_2$ thin film by hard x-ray photoemission spectroscopy (HAXPES) and soft x-ray absorption spectroscopy (XAS) as well as density functional theory (DFT)-based calculations. The core-level HAXPES spectra showed features characteristic of a Mott insulator. The DFT calculations predicted that Ru^{4+} in the $Sr_2RuO_3F_2$ thin film has a high-spin configuration with four unpaired *d* electrons and $Sr_2RuO_3F_2$ has an indirect band gap of 0.7 eV. Furthermore, the density of states (DOS) in the valence and conduction bands of the Sr_2RuO_4 and $Sr_2RuO_3F_2$ thin films were experimentally

*chikamatsu@chem.s.u-tokyo.ac.jp

analyzed by HAXPES and angular-dependent O 1*s* XAS measurements. By comparing the observed spectra with the results of the DFT calculations, we discuss the electronic structure of $Sr_2RuO_3F_2$ near the Fermi energy (E_F).

II. EXPERIMENT

Precursor Sr_2RuO_4 and fluorinated $Sr_2RuO_3F_2$ thin films were prepared on $LaAlO_3$ (001) (LAO, Shinkosha Co.) substrates by pulsed laser deposition (PLD) and successive topotactic fluorination using PVDF (Fluorochem Ltd.), as reported in our previous study [14]. The thicknesses of the Sr_2RuO_4 and $Sr_2RuO_3F_2$ thin films were ∼100 nm and ∼135 nm, respectively, as measured by x-ray reflectivity (Bruker AXS D8 DISCOVER). X-ray diffraction measurements confirmed that both of the thin films exhibited a K_2NiF_4-type structure with no impurity phases. HAXPES spectra were recorded at 300 K and vacuum pressure of 10^{-6} Pa using an R4000 electron energy analyzer (VG Scienta) installed at the BL47XU beam line of SPring-8. The incident photon energy was 7940 eV, which allowed bulk-sensitive spectroscopy to be performed with a probing depth of ∼10 nm. The total-energy resolution was set at 270 meV. The Fermi edge of an *in situ* evaporated gold film was used as the energy reference. XAS measurements were conducted using linear polarized light at the BL-2A beam line of the Photon Factory, KEK. The XAS spectra were measured at 300 K and vacuum pressure of $\sim 3 \times 10^{-8}$ Pa using the total electron-yield method. Before the XAS measurements, the films were rinsed with ethanol and then were kept in a high-vacuum atmosphere for more than 2 h to remove surface gas contaminants as much as possible.

DFT calculations were performed using the Vienna *ab initio* simulation package [15]. The generalized gradient approximation proposed by Perdew, Burke, and Ernzerhof (GGA-PBE) was adapted for the exchange correlation functional [16]. We treated on-site Coulomb repulsion between the Ru 4*d* electrons using the GGA + *U* method proposed by Dudarev *et al.* [17]. The effect of the core electrons was incorporated using a projector augmented wave (PAW) approach [18,19]. The cutoff energy was 600 eV for the valence electronic states composed of $4s^2 4p^6 5s^2$ electrons in Sr, $4p^6 4d^8 5s^2$ electrons in Ru, $2s^2 2p^4$ electrons in O, and $2s^2 2p^5$ electrons in F. The Brillouin-zone integration was carried out according to the Monkhorst-Pack **k**-point scheme [20]. We used $7 \times 7 \times 1$ and $3 \times 3 \times 1$ **k**-point meshes for $1 \times 1 \times 1$ and $\sqrt{2} \times \sqrt{2} \times 1$ supercells, respectively. We assumed an antiferromagnetic spin arrangement on Ru atoms, taking into consideration the experimental observation that $Sr_2RuO_3F_2$ exhibited no spontaneous magnetization [14]. The ionic positions and lattice constants were optimized so that the residual force on an atom and the pressure on the cell were smaller than 0.01 eV $Å^{-1}$ and 0.1 GPa, respectively. The crystal structures and wave functions were visualized using VESTA [21].

III. RESULTS AND DISCUSSION

A. Core-level photoemission spectra

Figure 1 shows the core-level HAXPES spectra of Ru 2*s*, 2*p*, and 3*p* and Sr 2*s*, 2*p*, and 3*d* for the Sr_2RuO_4 and $Sr_2RuO_3F_2$ thin films. As seen in Figs. 1(a)–1(e), the plasmon loss peaks were observed as satellites on the higher binding energy (E_b) side of the main core-level peaks [22]. The Ru 2*s*, 2*p*, and 3*p* core-level peaks of the Sr_2RuO_4 and $Sr_2RuO_3F_2$ thin films were located at the same E_b [Figs. 1(a)–1(c)], indicating that the Ru valence states of both films are tetravalent. On the other hand, as seen in Figs. 1(d)–1(f), the Sr 2*s*, 2*p*, and 3*d* peaks of the Sr_2RuO_4 thin film shifted by ∼0.7 eV towards higher E_b upon fluorination. The position of the Sr 3*d* peak is known to be strongly influenced by the surrounding anions (e.g., the Sr $3d_{5/2}$ peaks of SrO and SrF_2 are located at 132.6 eV and 133.85 eV, respectively) [23]. Thus, these shifts in the Sr core-level peaks are attributable to a change in the chemical environment around Sr upon F insertion.

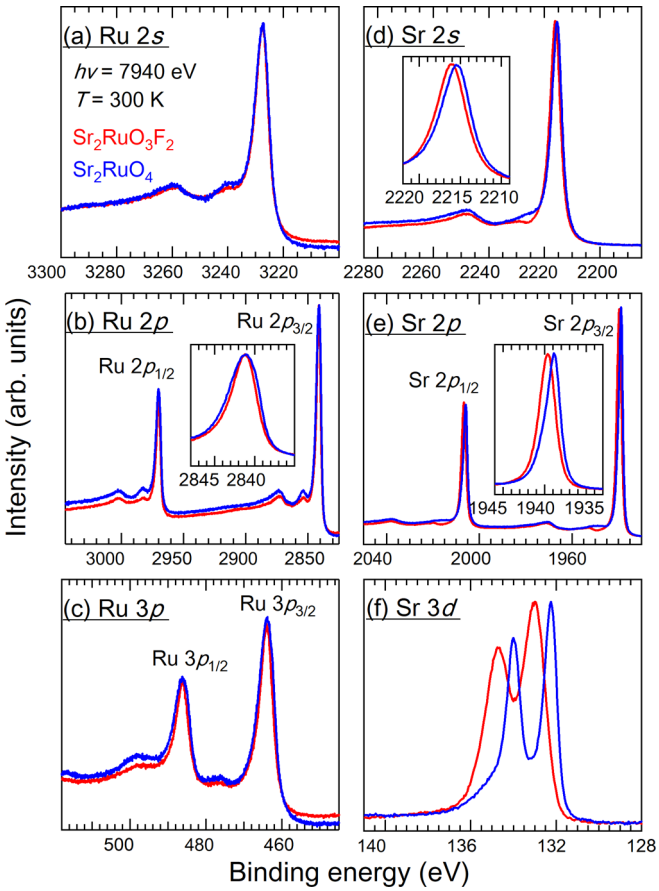

FIG. 1. Core-level HAXPES spectra of (a) Ru 2*s*, (b) Ru 2*p*, (c) Ru 3*p*, (d) Sr 2*s*, (e) Sr 2*p*, and (f) Sr 3*d* of the Sr_2RuO_4 and $Sr_2RuO_3F_2$ thin films. These spectra have been normalized to the maximum peak heights. The insets in (b), (d), and (e) show magnified views of Ru $2p_{3/2}$, Sr 2*s*, and Sr $2p_{3/2}$, respectively.

Figure 2 depicts the core-level spectra of Sr $3p_{1/2}$ and Ru 3*d* for the Sr_2RuO_4 and $Sr_2RuO_3F_2$ thin films; the intense Sr $3p_{1/2}$ peaks at an E_b of ∼279 eV and a Ru spin-orbit split doublet $3d_{5/2}$ and $3d_{3/2}$ in the E_b range of 280–291 eV are clearly resolved. The Ru 3*d* states overlap with the weak components of the C 1*s* states at an E_b of ∼285 eV, which originated due to surface-adsorbed contaminants such as carbon dioxides and hydrocarbon [24,25]. Upon fluorination, Sr $3p_{1/2}$ experienced

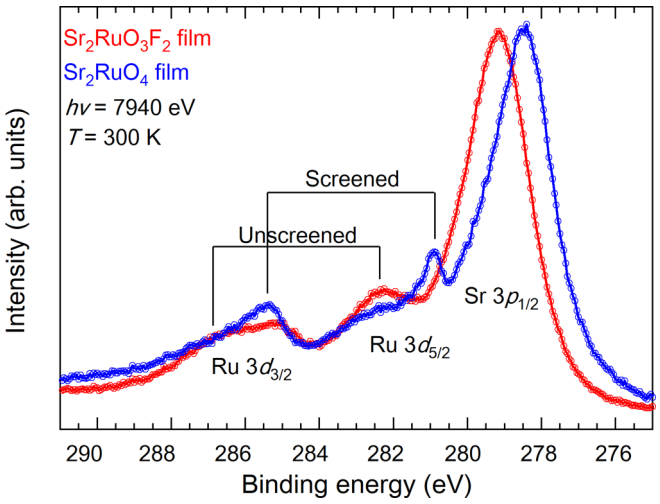

FIG. 2. Core-level spectra of Sr $3p_{1/2}$ and Ru $3d$ for the Sr_2RuO_4 and $Sr_2RuO_3F_2$ thin films. These spectra have been normalized to the maximum peak heights.

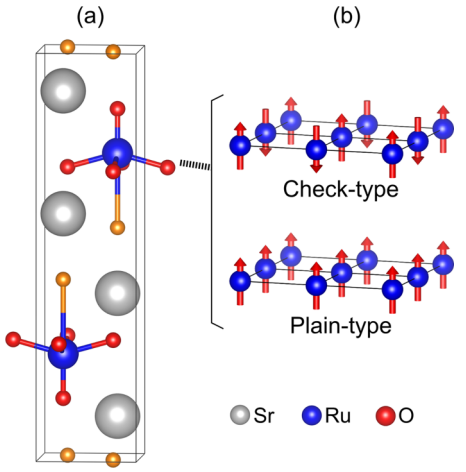

FIG. 3. (a) $Sr_2RuO_3F_2$ with $Sr_2TiO_3F_2$-type structure. (b) Two types of in-plane magnetic orderings of Ru spins. Upward and downward arrows denote up- and down-spin moment, respectively.

a peak shift of ∼0.7 eV towards higher E_b, which is in accordance with the shifts observed with Sr $2s$, $2p$, and $3d$ [Figs. 1(d)–1(f)]. Both the Ru $3d_{5/2}$ and $3d_{3/2}$ states of the Sr_2RuO_4 film had two components—a screened peak at a low E_b and a broad unscreened peak at a high E_b. The screened peaks of Ru $3d$ originate from the screening of a core hole by quasiparticles on the Fermi surface [26]. Similar peaks were found in the Ru $3d$ HAXPES spectrum of metallic $Sr_3Ru_2O_7$ [27]. In contrast, only unscreened peaks were observed in the Ru $3d_{5/2}$ and $3d_{3/2}$ states of the $Sr_2RuO_3F_2$ film. Oh *et al.* reported that the screened peaks of the Ru $3d$ states are absent in Mott insulators but appear at the lower E_b sides of the unscreened peaks when the correlation strength becomes weak and the system turns metallic [26]. Therefore, our observations on the Ru $3d$ states indicate that the Sr_2RuO_4 film is metallic while the $Sr_2RuO_3F_2$ film is a Mott insulator at 300 K; these observations are consistent with the results of the resistivity measurements [14].

B. Valence and conduction bands by theoretical calculations

In this section, we discuss the valence and conduction bands of $Sr_2RuO_3F_2$ using a theoretical approach. We optimized the lattice constants and atomic positions, assuming that $Sr_2RuO_3F_2$ has the same crystal structure as $Sr_2TiO_3F_2$ [28] [Fig. 3(a)]. We considered two types of in-plane ordering for Ru^{4+} spins, "check type" and "plain type" [Fig. 3(b)] and ignored interlayer orderings because our preliminary calculations showed that interlayer magnetic couplings were negligibly small (∼0.05 kJ/mol). Calculations were performed using the GGA + U method, where the U value was varied in a range of 0–7 eV to examine the U dependence of the results. Figure 4(a) shows the c-axis lengths of $Sr_2RuO_3F_2$ obtained for the two magnetic orderings and a series of U values. Notably, optimization starting with different initial c-axis lengths resulted in different structures. As seen from the figure, five structure phases with different c-axis lengths were predicted: check-A, -B, -C and plain-A, -B. Among them, check-A and plain-A, which appeared at U larger than 4 eV, well reproduce the experimental c length (16.7 Å). Figure 4(b) compares the relative energy of the five phases. The most stable phase was plain-B and the second one was check-A when $U > 4.5$ eV. These results suggest that the metastable check-A phase was formed in the $Sr_2RuO_3F_2$ film.

U values around 2 eV have been used for first-principles calculation of Ru oxides [29–32]. However, the experimental lattice constants of the $Sr_2RuO_3F_2$ film were reproduced only when U is larger than 4 eV. To confirm the validity of such a high-U value, we calculated U using the first-principles method proposed by Cococcioni *et al.* [33],

$$U = \left(\chi_{\rm nsc}^{-1} - \chi_{\rm sc}^{-1}\right)_{ii}, \quad \chi_{ij} = \frac{\partial n_i}{\partial \alpha_j}. \tag{1}$$

Here, n_i is the occupation number of Ru-d orbitals at site i and α_j is the artificial potential applied on another Ru site j, at which the energy level of the d orbitals is shifted. χ is the response of the site occupation n to a potential shift α. The subscripts "nsc" and "sc" stand for non-self-consistent and self-consistent, respectively. To calculate $\chi_{\rm nsc}$, the charge density of the ground state ($\alpha = 0$) was used as a fixed parameter, while the charge density in the $\chi_{\rm sc}$ calculation was

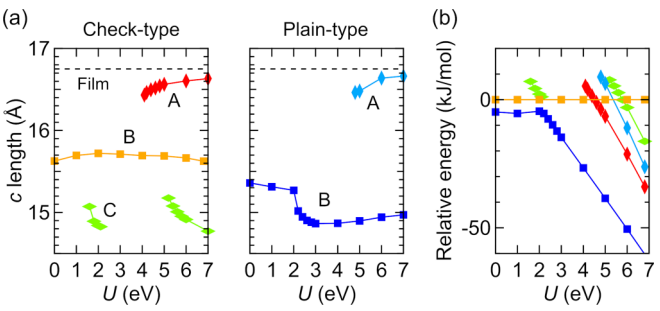

FIG. 4. (a) c-axis lengths of $Sr_2RuO_3F_2$ calculated for various U values. The figures indicate five different phases: check-A, -B, -C and plain-A, -B. The experimental c-axis value is shown by a broken line. (b) Relative energy of the five phases as a function of U.

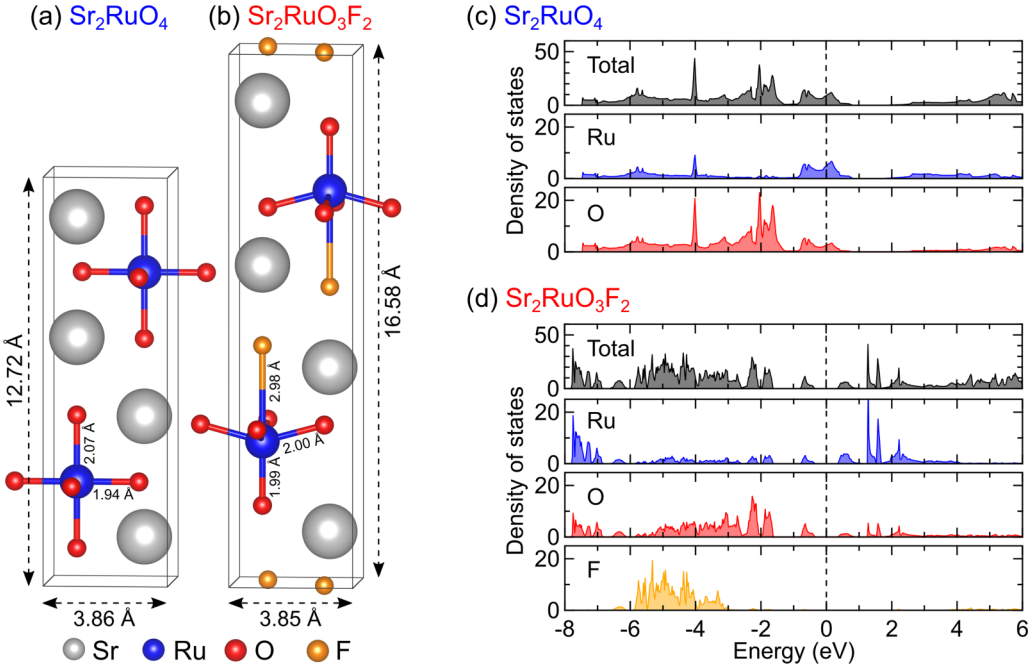

FIG. 5. (a) The reported crystal structure of Sr_2RuO_4 in Ref. [33] and (b) the structure of $Sr_2RuO_3F_2$ calculated by the GGA + U method. The lattice constants and Ru-O/F bond lengths (Å) are shown in the figures. Total and site-projected DOS for (c) Sr_2RuO_4 and (d) $Sr_2RuO_3F_2$. The vertical dashed lines in (c) and (d) denote E_F.

updated with respect to the applied potential α [33]. By this method, the U value was found to be 6.0 eV.

Figures 5(a) and 5(b) depict the crystal structure of Sr_2RuO_4 reported by Huang *et al.* [34] and the check-A structure of $Sr_2RuO_3F_2$ calculated by the GGA + U method. The calculated lattice constants are in good agreement with the experimentally measured constants (a = 3.86 Å and c = 16.75 Å) [14]. As shown in Fig. 5(b), the center Ru cation in the RuO_5F octahedra of $Sr_2RuO_3F_2$ is displaced towards the more negative O^{2-} than F^-. As a result, the Ru-O bond lengths are as short as ∼2 Å, being almost the same as those in Sr_2RuO_4 [Fig. 5(a)] [34], whereas the Ru-F bond distance is elongated up to ∼3 Å.

Figure 5(c) depicts the DOS of Sr_2RuO_4 obtained by the GGA + U calculation, where the reported crystal structure [34], paramagnetism [35], and U value of 5.3 eV estimated from Eq. (1) were used. As seen in Fig. 5(c), the valence band of Sr_2RuO_4 is composed of Ru $4d t_{2g}$-derived states crossing E_F, O $2p$ bands located at −1.3 to −3.5 eV, isolated p_z orbitals of apical oxygen atoms hybridized with the Ru $4d_{3z^2-r^2}$ orbital around −4 eV, and Ru $4d$ and O $2p$ derived states located at −4.2 to −7 eV. The valence band qualitatively reproduced a previous calculation accomplished by local-density approximation (LDA) [36]. Figure 5(d) shows the calculated DOS for $Sr_2RuO_3F_2$. Remarkably, a finite gap opened at E_F and the Ru $4d$ states moved to the bottom of the valence bands near −8 eV. Furthermore, the F $2p$ states appeared at −3 to −6.5 eV; they were almost isolated and not hybridized with the Ru $4d$ states, reflecting the long bond distance between Ru and F.

In order to investigate the d electron configuration of $Ru^{4+}(d^4)$ in Sr_2RuO_4 and $Sr_2RuO_3F_2$, we calculated the partial DOS (PDOS) of Ru d_{xy}, $d_{yz} + d_{zx}$, $d_{3z^2-r^2}$, and $d_{x^2-y^2}$ bands, as shown in Fig. 6. Ru^{4+} oxides with octahedral geometry are usually a low-spin configuration $(xy, yz, zx)^{\uparrow\uparrow\uparrow\downarrow}$, such as $SrRuO_3$ and Ca_2RuO_4 [37,38], or non-spin-polarized $(xy, yz, zx)^4$, such as Sr_2RuO_4 and RuO_2 [35,39]. In these compounds, the fourth d electron occupies not an e_g band, but a t_{2g} band, due to the large crystal-field splitting between the t_{2g} and e_g orbitals. Figure 6(a) shows PDOS for Sr_2RuO_4. It depicts the $(t_{2g})^4$ configuration, as reported in Ref. [32]. However, PDOS for $Sr_2RuO_3F_2$ [Fig. 6(b)] suggests the Ru^{4+} exhibited a high-spin configuration, $(xy)^{\uparrow}(yz, zx)^{\uparrow\uparrow}(3z^2 - r^2)^{\uparrow}$. This anomalous occupation of the $(3z^2 - r^2)^{\uparrow}$ orbital would be due to the change in crystal field around the Ru atoms. Figure 6(c) shows the local geometries around Ru of the two compounds shown in Figs. 5(a) and 5(b), and the schematic energy diagrams for the d orbitals. Sr_2RuO_4 has almost regular RuO_6 octahedra and well-separated t_{2g} and e_g orbitals, and all four d electrons of Sr_2RuO_4 occupy the t_{2g} band. On the other hand, $Sr_2RuO_3F_2$ has long Ru-F bond distance, which makes the coordination geometry of the Ru square pyramidal-like rather than octahedral, and thus stabilizes the $4d_{3z^2-r^2}$ orbital. As a result, the fourth electron occupies the $4d_{3z^2-r^2}$ orbital, and the whole configuration becomes the high-spin state.

Figure 7 shows the calculated band dispersion of $Sr_2RuO_3F_2$ with the Brillouin zone for a simple tetragonal lattice. As seen in the figure, $Sr_2RuO_3F_2$ has little dispersion along the $\Gamma - Z$ path and the band structures along $\Gamma - X - M (k_z = 0)$ and $Z - R - A (k_z = 1/2)$ are almost identical because of the long c axis. The valence band maximum is located at the points M and A, while the conduction minimum is at X and R, suggesting that $Sr_2RuO_3F_2$ has an indirect

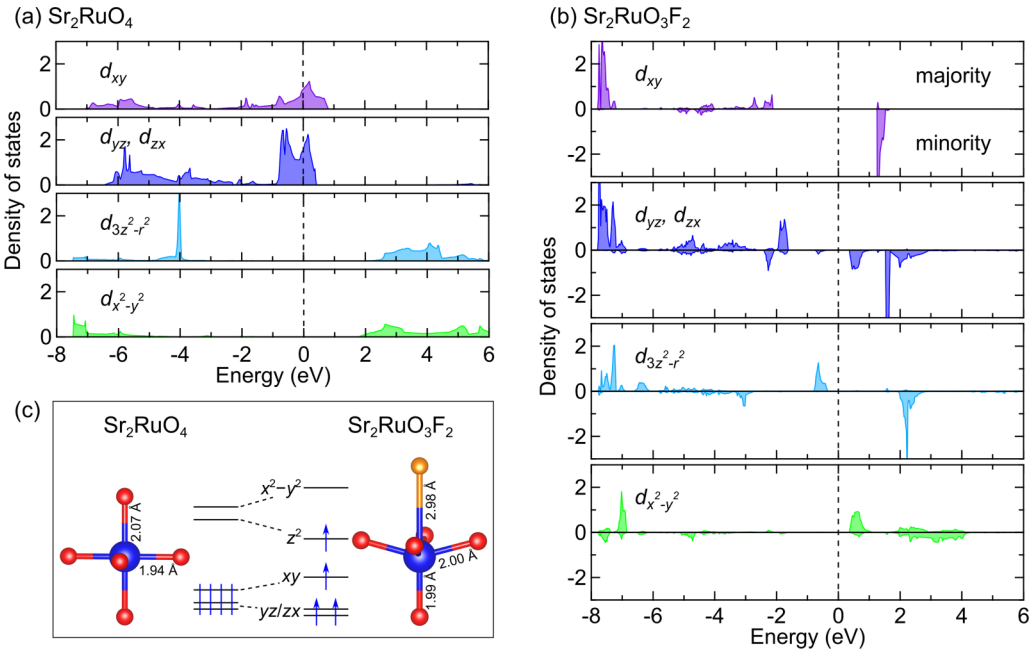

FIG. 6. PDOS for the Ru-4d electrons in (a) Sr_2RuO_4 and (b) $Sr_2RuO_3F_2$. The lines in positive and negative regions denote the PDOS of the majority and minority of spin electrons, respectively. (c) The local structures around Ru in Sr_2RuO_4 and $Sr_2RuO_3F_2$, and the schematic diagrams for $4d^4$ configurations under the two types of crystal field.

band gap. The width of the band gap was estimated to be 0.7 eV.

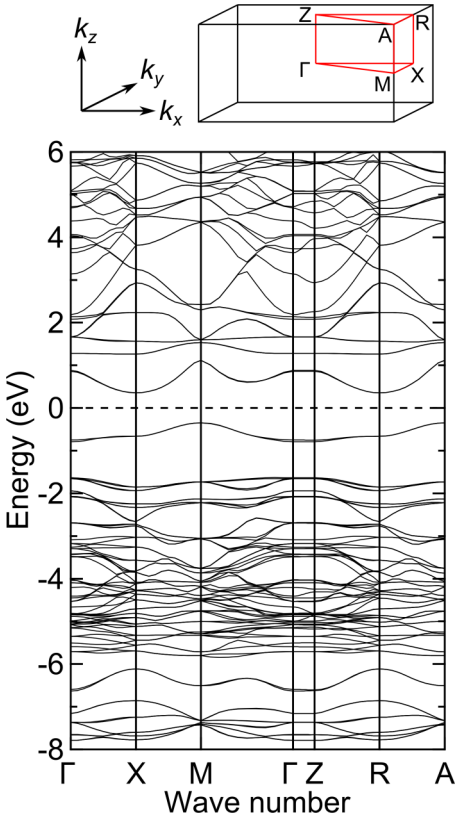

FIG. 7. Band dispersion image of $Sr_2RuO_3F_2$ and the Brillouin zone for a simple tetragonal lattice; the critical points are denoted. The horizontal dashed line in the lower illustration denotes E_F.

C. Valence and conduction bands by x-ray photoemission and absorption spectroscopy

The electronic structures of the valence and conduction bands of Sr_2RuO_4 and $Sr_2RuO_3F_2$ were experimentally probed by x-ray photoemission and absorption spectroscopic analyses as well. Figure 8 shows the valence band spectra of the Sr_2RuO_4 and $Sr_2RuO_3F_2$ thin films. Although the experimentally observed valence bands in Fig. 8 were broader and extend more towards the higher E_b side than the theoretical

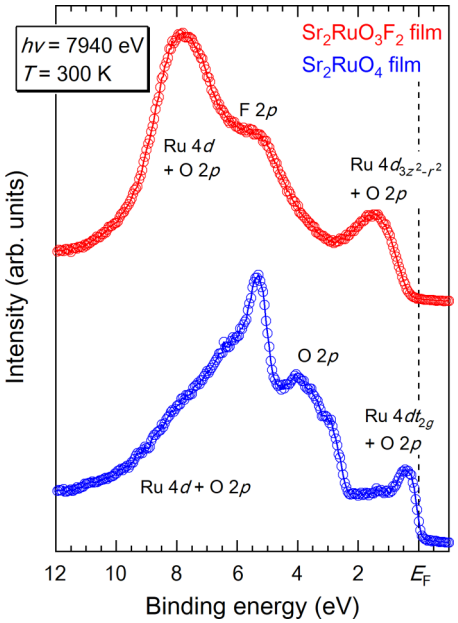

FIG. 8. Valence band spectra of the Sr_2RuO_4 and $Sr_2RuO_3F_2$ thin films. The spectra have been normalized to the area from −1 to 12 eV.

ones in Figs. 5(c) and 5(d), we can assign the characteristic structures seen in the valence band spectra according to our GGA + U calculations and previously reported LDA calculations and PES measurements [36,40] as follows. In the spectrum of the Sr_2RuO_4 thin film, the area located at E_F to ~2 eV was identified as the Ru $4dt_{2g}$ states hybridized with O $2p$, the area at ~2−4.6 eV as O $2p$ derived states, the peak at 5.3 eV as isolated p_z orbitals of the apical oxygen atoms hybridized with the Ru $4d_{3z^2-r^2}$ orbital, and the area located at ~6−10 eV as the Ru $4d$ and O $2p$ hybridized states, respectively. Particularly, the peak at ~0.4 eV with a sharp Fermi edge and the broad band at ~1−2 eV in the Ru $4d$ t_{2g} states are assigned as the coherent and incoherent parts of the spectral function, respectively, based on a comparison with the valence band spectrum of $SrRuO_3$ [41]. On the other hand, the spectrum of the $Sr_2RuO_3F_2$ film showed no DOS at E_F, which is consistent with the insulating resistivity behavior [14]. By comparing Fig. 5(d) and Fig. 6(b), the peaks centered at E_b = 1.5,5.5, and 7.8 eV are assigned to Ru $4d_{3z^2-r^2}$ hybridized with O $2p$, F $2p$ derived states, and Ru $4d$ states hybridized with O $2p$, respectively.

Finally, to examine the conduction band structure of the Sr_2RuO_4 and $Sr_2RuO_3F_2$ thin films, we measured the O $1s$ XAS spectra using polarized light. In this measurement, the O $1s$ electrons are excited into unoccupied $2p$ orbitals hybridized with Ru $4d$ orbitals. Due to the dipole selection rule, the direction of the $2p$ orbitals to which the $1s$ electrons are transferred depends on the angle between the incident beam and the surface normal (θ_{inc}) [42]. When θ_{inc} is zero, $1s$ electrons are transferred to the $2p_x$ or $2p_y$ orbital. The final state gradually changes to $2p_z$ as θ_{inc} increases up to 90°. Therefore, the position of the XAS peak and its θ_{inc} dependence indicate the energy position of the Ru $4d$ states and the direction of the O $2p$ orbitals (p_x,p_y, and p_z), respectively. Figure 9 exhibits the XAS spectra measured at θ_{inc} = 0°,30°, and 60°. The angular dependence of the O $1s$ XAS spectra could be clearly observed for both the Sr_2RuO_4 and $Sr_2RuO_3F_2$ films.

The results obtained for the Sr_2RuO_4 film are in good agreement with those reported previously on a Sr_2RuO_4 (001) single crystal prepared by *in situ* cleaving at 160 K [42]. The peak at 528.2 eV (structure A) decreased with increasing θ_{inc}, while the peak at 529.2 eV (structure B) considerably increased with θ_{inc}. According to Ref. [42], structure A is assigned to the $2p_x$ and $2p_y$ states of the apical oxygen hybridized with Ru $4d_{yz}$ and $4d_{zx}$ and structure B is a combination of the $2p_x$,$2p_y$, and $2p_z$ states of the in-plane oxygen hybridized with the Ru $4d$ t_{2g} orbitals. The weight of A from the apical oxygen was much smaller than that of B from the in-plane oxygen, reflecting the two-times-smaller amount of the apical oxygen than the in-plane one. The structures C and D at ~ 531 and 533.1 eV are derived from Ru $4d$ with e_g symmetry ($d_{3z^2-r^2}$ and $d_{x^2-y^2}$) hybridized with both apical and in-plane O $2p\sigma$ states.

On the other hand, as seen in Fig. 9(b), the behavior of the O $1s$ spectra of the $Sr_2RuO_3F_2$ film was different from that of the Sr_2RuO_4 film. The peaks at 528.6 and 532.0 eV (structures E and H) were observed at θ_{inc} = 0°. With increasing θ_{inc}, the intensities of E and H slightly decreased and prominent peaks at 530.2 and 531.2 eV (structures F and G) evolved. Such θ_{inc} dependence suggests that the peaks E and H arise from the Ru $4d$ orbitals hybridized with the $2p_x$,$2p_y$, and $2p_z$

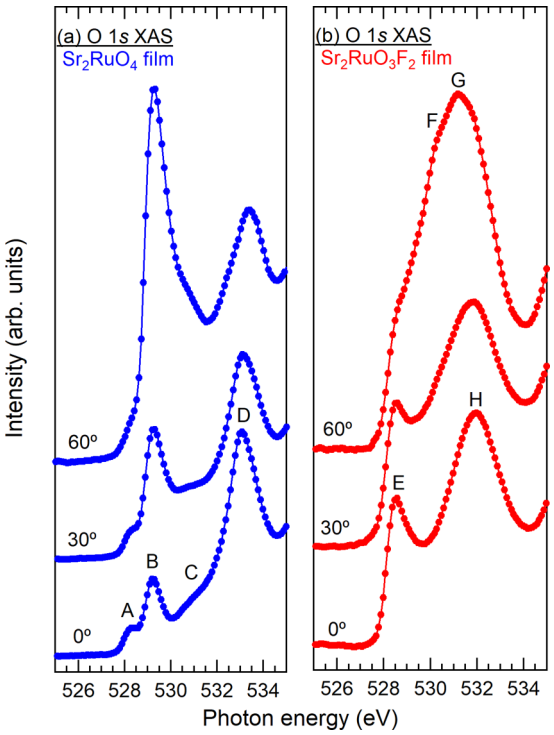

FIG. 9. O $1s$ XAS spectra of (a) Sr_2RuO_4 and (b) $Sr_2RuO_3F_2$ films. The spectra are shown at θ_{inc} = 0°,30°, and 60°; θ_{inc} is the angle between the incident beam and the surface normal. The structures labeled A to H are discussed in the text.

orbitals of the in-plane oxygen atoms and F and G arise from the $4d$ orbitals hybridized with the $2p_z$ orbitals of the in-plane oxygen. The weak peaks from the apical oxygen are possibly hidden by the intense peaks from the in-plane oxygen. The $4d$ orbitals responsible for F and G are hybridized with the $2p_z$ orbital in-plane oxygen only and thus they can be assigned to the Ru $4d_{yz}$ and Ru $4d_{zx}$ orbitals. The Ru $4d$ orbitals related to the structures E and H are hybridized with all the $2p_x$,$2p_y$, and $2p_z$ orbitals of the in-plane oxygen. The calculated PDOS for the Ru $4d$ states shown in Fig. 6(b) suggests that the conduction band minima, corresponding to peak E, are derived from $4d_{yz}$,$4d_{zx}$, and $4d_{x^2-y^2}$ and that the highest $4d$ band (peak H) is attributable to $4d_{x^2-y^2}$. It should be noted that $4d_{x^2-y^2}$ can be hybridized with not only $2p_x$ and $2p_y$, but also the $2p_z$ orbital of the in-plane oxygen because the Ru atom is displaced toward the apical oxygen and the $O_{in-plane}$−Ru−$O_{in-plane}$ bond angle is not 180°, as illustrated in Fig. 5(b).

IV. CONCLUSION

The electronic structure of a $Sr_2RuO_3F_2$ thin film was investigated by HAXPES and XAS as well as GGA + U calculations. The core-level HAXPES spectra of the $Sr_2RuO_3F_2$ film showed features characteristic of a Mott insulator. The GGA + U calculations predicted that $Sr_2RuO_3F_2$ has a high-spin Ru(IV) configuration and an indirect band gap of 0.7 eV with minima at the M,A and X,R points. Moreover, the valence band and conduction band DOS of the $Sr_2RuO_3F_2$ thin film, as measured by HAXPES near the E_F and angular-dependent O $1s$ XAS, differed substantially from those of the Sr_2RuO_4 film. This electronic modification is possibly driven by the

substitution of oxygen atoms coordinated to Ru by fluorine and the resulting crystal-field deviation. These findings can help one to understand the physical properties of both known and unknown ruthenium oxyfluorides from the perspective of crystal and electronic structures.

ACKNOWLEDGMENTS

This work was partially supported by the Core Research for Evolutionary Science and Technology of the Japan Science and Technology Agency and by Grants-in-Aid for Scientific Research (Grants No. 15H05424 and No. 16H06441) from the Japan Society for the Promotion of Science (JSPS). Synchrotron radiation experiments were performed with the approval of the Photon Factory Program Advisory Committee, KEK (Proposals No. 2015G577 and No. 2015S2-005) and at BL47XU of the SPring-8 facility with the approval of the Japan Synchrotron Radiation Research Institute (JASRI) (Proposals No. 2015B1799 and No. 2016A1221).

[1] A. Callaghan, C. W. Moeller, and R. Ward, Inorg. Chem. **5**, 1572 (1966).
[2] Y. Maeno, H. Hashimoto, K. Yoshida, S. Nishizaki, T. Fujita, J. G. Bednorz, and F. Lichtenberg, Nature (London) **372**, 532 (1994).
[3] A. P. Mackenzie, R. K. W. Haselwimmer, A. W. Tyler, G. G. Lonzarich, Y. Mori, S. Nishizaki, and Y. Maeno, Phys. Rev. Lett. **80**, 3890 (1998).
[4] R. S. Perry, L. M. Galvin, S. A. Grigera, L. Capogna, A. J. Schofield, A. P. Mackenzie, M. Chiao, S. R. Julian, S. I. Ikeda, S. Nakatsuji, Y. Maeno, and C. Pfleiderer, Phys. Rev. Lett. **86**, 2661 (2001).
[5] Y. Maeno, S. Nakatsuji, and S. Ikeda, Mater. Sci. Eng. B **63**, 70 (1999).
[6] L. Pi, A. Maignan, R. Retoux, and B. Raveau, J. Phys.: Condens. Matter **14**, 7391 (2002).
[7] R. Nithya, V. S. Sastry, P. Paul, T. C. Han, J. G. Lin, and F. C. Chou, Solid State Commun. **149**, 1674 (2009).
[8] B. Dabrowski, S. Kolesnik, O. Chmaissem, T. Maxwell, M. Avdeev, P. W. Barnes, and J. D. Jorgensen, Phys. Rev. B **72**, 054428 (2005).
[9] Z. H. Han, J. I. Budnick, W. A. Hines, B. Dabrowski, S. Kolesnik, and T. Maxwell, J. Phys.: Condens. Matter **17**, 1193 (2005).
[10] A. J. Williams, A. Gillies, J. P. Attfield, G. Heymann, H. Huppertz, M. J. Martínez-Lope, and J. A. Alonso, Phys. Rev. B **73**, 104409 (2006).
[11] V. Durairaj, S. Chikara, X. N. Lin, A. Douglass, G. Cao, P. Schlottmann, E. S. Choi, and R. P. Guertin, Phys. Rev. B **73**, 214414 (2006).
[12] K. Kurita, A. Chikamatsu, K. Shigematsu, T. Katayama, H. Kumigashira, T. Fukumura, and T. Hasegawa, Phys. Rev. B **92**, 115153 (2015).
[13] R. K. Li and C. Greaves, Phys. Rev. B **62**, 3811 (2000).
[14] K. Kawahara, A. Chikamatsu, T. Katayama, T. Onozuka, D. Ogawa, K. Morikawa, E. Ikenaga, Y. Hirose, I. Harayama, D. Sekiba, T. Fukumura, and T. Hasegawa, CrystEngComm **19**, 313 (2017).
[15] G. Kresse and J. Furthmüller, Phys. Rev. B **54**, 11169 (1996).
[16] J. P. Perdew, K. Burke, and M. Ernzerhof, Phys. Rev. Lett. **77**, 3865 (1996).
[17] S. L. Dudarev, G. A. Botton, S. Y. Savrasov, C. J. Humphreys, and A. P. Sutton, Phys. Rev. B **57**, 1505 (1998).
[18] P. E. Blöchl, Phys. Rev. B **50**, 17953 (1994).
[19] G. Kresse and D. Joubert, Phys. Rev. B **59**, 1758 (1999).
[20] H. J. Monkhorst and J. D. Pack, Phys. Rev. B **13**, 5188 (1976).
[21] K. Momma and F. Izumi, J. Appl. Crystallogr. **44**, 1272 (2011).
[22] M. Fondell, M. Gorgoi, M. Boman, and A. Lindblad, Results Phys. **4**, 168 (2014).
[23] R. P. Vasquez, J. Electron Spectrosc. Relat. Phenom. **56**, 217 (1991).
[24] C. Russo and R. Kaplow, Surf. Sci. **69**, 453 (1977).
[25] S. Suzuki *et al.*, Mater. Trans. **36**, 1379 (1995).
[26] H. D. Kim, H. J. Noh, K. H. Kim, and S. J. Oh, Phys. Rev. Lett. **93**, 126404 (2004).
[27] G. Panaccione, U. Manju, F. Offi, E. Annese, I. Vobornik, P. Torelli, Z. H. Zhu, M. A. Hossain, L. Simonelli, A. Fondacaro, P. Lacovig, A. Guarino, Y. Yoshida, G. A. Sawatzky, and A. Damascelli, New J. Phys. **13**, 053059 (2011).
[28] P. R. Slater and R. K. B. Gover, J. Mater. Chem. **12**, 291 (2002).
[29] Z. V. Pchelkina, I. A. Nekrasov, T. Pruschke, A. Sekiyama, S. Suga, V. I. Anisimov, and D. Vollhardt, Phys. Rev. B **75**, 035122 (2007).
[30] S. Ryee, S. W. Jang, H. Kino, T. Kotani, and M. J. Han, Phys. Rev. B **93**, 075125 (2016).
[31] T. T. Tran, T. Mizokawa, S. Nakatsuji, H. Fukazawa, and Y. Maeno, Phys. Rev. B **70**, 153106 (2004).
[32] V. I. Anisimov, I. A. Nekrasov, D. E. Kondakov, T. M. Rice, and M. Sigrist, Eur. Phys. J. B **25**, 191 (2002).
[33] M. Cococcioni and S. de Gironcoli, Phys. Rev. B **71**, 035105 (2005).
[34] Q. Huang, J. L. Soubeyroux, O. Chmaissem, I. N. Sora, A. Santoro, R. J. Cava. J. J. Krajewski, and W. F. Peck Jr., J. Solid State Chem. **112**, 355 (1994).
[35] S. Nakatsuji and Y. Maeno, Phys. Rev. Lett. **84**, 2666 (2000).
[36] T. Oguchi, Phys. Rev. B **51**, 1385 (1995).
[37] A. Kanbayasi, J. Phys. Soc. Jpn. **41**, 1876 (1976).
[38] M. Braden, G. Andre, S. Nakatsuji and Y. Maeno, Phys. Rev. B **58**, 847 (1998).
[39] W. D. Ryden and A. W. Lawson, J. Chem. Phys. **52**, 6058 (1970).
[40] T. Yokoya, A. Chainani, T. Takahashi, H. Katayama-Yoshida, M. Kasai, Y. Tokura, N. Shanthi, and D. D. Sarma, Phys. Rev. B **53**, 8151 (1996).
[41] M. Takizawa, D. Toyota, H. Wadati, A. Chikamatsu, H. Kumigashira, A. Fujimori, M. Oshima, Z. Fang, M. Lippmaa, M. Kawasaki, and H. Koinuma, Phys. Rev. B **72**, 060404 (2005).
[42] M. Schmidt, T. R. Cummins, M. Bürk, D. H. Lu, N. Nücker, S. Schuppler, and F. Lichtenberg, Phys. Rev. B **53**, R14761 (1996).